J Therm Anal Calorim (2012) 109:163–169
DOI 10.1007/s10973-011-1577-7

Selective self-assembly synthesis of $MnV_2O_6{\cdot}4H_2O$ with controlled morphologies and study on its thermal decomposition

Xuehang Wu · Wenwei Wu · Xuemin Cui · Sen Liao

Received: 20 February 2011 / Accepted: 7 April 2011 / Published online: 16 April 2011

Abstract The $MnV_2O_6{\cdot}4H_2O$ with rod-like morphologies was synthesized by solid-state reaction at low heat using $MnSO_4{\cdot}H_2O$ and NH_4VO_3 as raw materials. XRD analysis showed that $MnV_2O_6{\cdot}4H_2O$ was a compound with monoclinic structure. Magnetic characterization indicated that $MnV_2O_6{\cdot}4H_2O$ and its calcined products behaved weak magnetic properties. The thermal process of $MnV_2O_6{\cdot}4H_2O$ experienced three steps, which involves the dehydration of the two waters of crystallization at first, and then dehydration of other two waters of crystallization, and at last melting of MnV_2O_6. In the DSC curve, the three endothermic peaks were corresponding to the two steps thermal decomposition of $MnV_2O_6{\cdot}4H_2O$ and melting of MnV_2O_6, respectively. Based on the Kissinger equation, the average values of the activation energies associated with the thermal decomposition of $MnV_2O_6{\cdot}4H_2O$ were determined to be 55.27 and 98.30 kJ mol^{-1} for the first and second dehydration steps, respectively. Besides, the thermodynamic function of transition state complexes ($\Delta H^{\neq}$, $\Delta G^{\neq}$, and $\Delta S^{\neq}$) of the decomposition reaction of $MnV_2O_6{\cdot}4H_2O$ were determined.

Keywords Inorganic compounds · Chemical synthesis · Non-isothermal kinetics · Thermodynamics · Thermal decomposition

Introduction

It is well known that the cathode materials in rechargeable Li-ion batteries commercially used are the layered rock salt oxides, such as Li_xCoO_2, Li_xNiO_2, $Li_xMn_2O_4$, $Li_xNi_{0.8}Co_{0.2}O_2$, $Li_x(Ni_{0.8}Co_{0.15}Al_{0.05})O_2$, and $Li_y[Ni_xCo_{1-2x}Mn_x]O_2$ [1–5], and anode materials are graphite. However, the graphite anode material commonly used in Li-ion rechargeable batteries suffers from small capacity per unit weight (about 350 mAh g^{-1}) and/or per unit volume due to its low density [6]. To overcome these disadvantages, considerable amounts of attempts have been made by many researchers to find out alternative anode materials in place of graphite anodes, and some progress has been made. Recently, bivalent transition metal vanadates with brannerite structure MV_2O_6 (M = Zn, Mn, Co, Cu, and Ni) compounds have been promoted as alternative anode of lithium ion rechargeable batteries [7–10], which is attributed to its higher discharge capacity, excellent recyclability, thermal stability, low-cost, and environmental benefits. Therein, synthesis and electrochemical properties of MnV_2O_6 have been widely investigated.

To date, various methods have been developed to synthesize crystalline MnV_2O_6 compounds, including solid-state reaction [11, 12], coprecipitation [13–15], hydrothermal method [16, 17], microwave radiation [18], polymer gelatin method [6], etc. It was found that MnV_2O_6 morphologies associated with electrochemical performance were highly dependent on the synthesis and processing methods, such as, Huang et al. [19] obtained nanobelts MnV_2O_6 via hydrothermal method, which exhibits a very reversible discharge/charge capacity and excellent cycling stability even at a current density as high as 1 A g^{-1}. Kim et al. [6] obtained spherical MnV_2O_6 crystalline by a polymer gelatin method, and observed a large capacity of about 1400 mAh g^{-1} during the first charge. Morishita et al. [15] synthesized rod-like MnV_2O_6 by coprecipitation method, and obtained both charge and discharge capacities of more than 600 mAh g^{-1} and about 100% columbic efficiency beyond 25 cycles.

X. Wu · W. Wu (✉) · X. Cui · S. Liao
School of Chemistry and Chemical Engineering, Guangxi University, Nanning 530004, China
e-mail: gxuwuwenwei@yahoo.com.cn

The aim of this study is to prepare $MnV_2O_6{\cdot}4H_2O$ with controlled morphologies via solid-state reaction at low heat [20, 21] and to study the kinetics and thermodynamics of the decomposition of $MnV_2O_6{\cdot}4H_2O$ using DSC technique. Non-isothermal kinetics of the decomposition process of $MnV_2O_6{\cdot}4H_2O$ was interpreted by the Kissinger method [22]. The kinetic (E_a, ln$A$) and thermodynamic functions ($\Delta H^{\neq}$, $\Delta S^{\neq}$, $\Delta G^{\neq}$) of the decomposition reaction of $MnV_2O_6{\cdot}4H_2O$ are discussed for the first time.

Experimental

Reagent and apparatus

All chemicals were of reagent grade purity. TG/DSC measurements were made using a Netsch 40PC thermogravimetric analyzer. X-ray powder diffraction (XRD) was performed using a Rigaku D/max 2500 V diffractometer equipped with a graphite monochromator and a Cu target. The FT-IR spectra of the product and its calcined product were recorded on a Nexus 470 FT-IR instrument. The morphologies of the product and its calcined samples were examined by S-3400 scanning electron microscopy (SEM). The magnetic properties of the compound powder were carried out at room temperature using a magnetic property measurement system (SQUID-MPMS-XL-5).

Preparation of $MnV_2O_6{\cdot}4H_2O$

NH_4VO_3 and $MnSO_4{\cdot}H_2O$ were employed for the preparation of the title compounds. NH_4VO_3 and $MnSO_4{\cdot}H_2O$ were added in the molar ratio of 2:1 and grinded in a mortar by hand with a rubbing mallet for 40 min in the presence of surfactant polyethylene glycol (PEG)-400. The grinding velocity was about 95 circles/min, and the strength applied was moderate. The mixture was washed with water to remove soluble inorganic salts until SO_4^{2-} ion could not be visually detected with a 0.5 mol L^{-1} $BaCl_2$ solution. The solid was then washed with a small amount of anhydrous ethanol and dried at 353 K for 3 h. The resulting material was subsequently determined to be the single phase $MnV_2O_6{\cdot}4H_2O$.

Method of determining kinetic parameters and thermodynamics functions

Determination of activation energy and pre-exponential factor by Kissinger method [22]

According to DSC analysis and the Kissinger equation (Eq. 1), the activation energy and pre-exponential factor of thermal decomposition reaction of $MnV_2O_6{\cdot}4H_2O$ can be obtained.

$$\ln\frac{\beta}{T_P^2} = -\frac{E_a}{RT_P} + \ln\frac{AR}{E_a} \tag{1}$$

where β is the heating rate (K min^{-1}); T_P is the peak temperature of DSC curve (K); E_a is the activation energy (kJ mol^{-1}) of thermal process; R is the gas constant (8.314 J mol^{-1} K^{-1}), and A is the pre-exponential factor. The dependence of $\ln(\beta/T_P^2)$ on $1/T_P$ must give rise to a straight line. Thus, reaction activation energy E_a can be obtained from linear slope ($-E_a/R$), and the pre-exponential factor A can be obtained from linear intercept (ln (AR/E_a)).

Determination of thermodynamic functions of thermal decomposition reaction [23, 24]

The change of the entropy ($\Delta S^{\neq}$) of thermal decomposition reaction for $MnV_2O_6{\cdot}4H_2O$ may be calculated according to the Eq. 2:

$$\Delta S^{\neq} = R\ln\left(\frac{Ah}{e\chi k_B T_P}\right) \tag{2}$$

where A is the pre-exponential factor obtained from the Kissinger method; $e = 2.7183$ is the Neper number; χ is the transition factor, which is unity for monomolecular reactions; k_B is the Boltzmann constant (1.381×10^{-23} J K^{-1}); h is the Plank constant (6.626×10^{-34} J s); T_P is the peak temperature of DSC curve; R is the gas constant (8.314 J mol^{-1} K^{-1}).

The change of the enthalpy ($\Delta H^{\neq}$) of thermal decomposition reaction for $MnV_2O_6{\cdot}4H_2O$ may be obtained according to the Eq. 3:

$$\Delta H^{\neq} = E^{\neq} - RT_P \tag{3}$$

where $E^{\neq}$ is the activation energy, E_a, obtained from the Kissinger method. The change of Gibbs free energy $\Delta G^{\neq}$ for the decomposition reaction of $MnV_2O_6{\cdot}4H_2O$ can be calculated using the well-known thermodynamic Eq. 4:

$$\Delta G^{\neq} = \Delta H^{\neq} - T_P\Delta S^{\neq} \tag{4}$$

Results and discussion

XRD analysis of the product and its calcined samples

Figure 1 shows the XRD patterns of the product dried at 353 K and the products resulting from calcination at different temperatures for 2 h.

From Fig. 1a, the results show that strong intensity and smoothed baseline, a wide and low diffraction pattern of

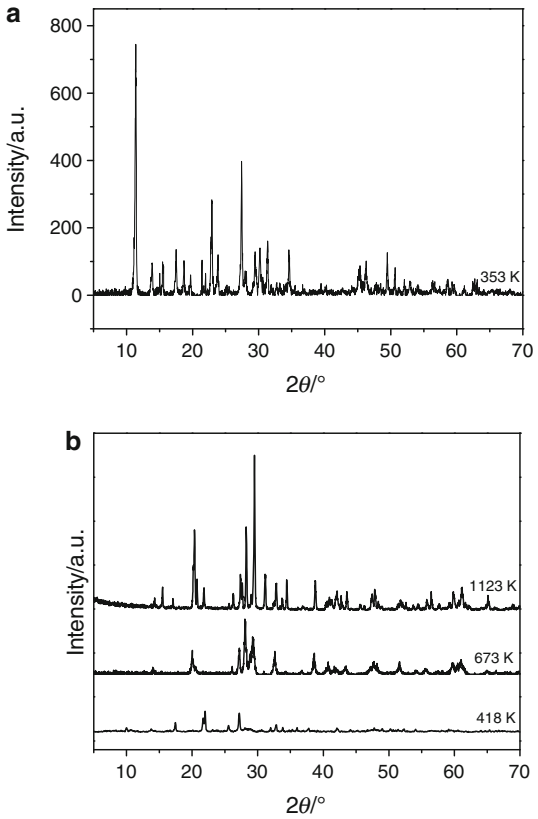

Fig. 1 XRD patterns of the synthesized sample (**a**) and its calcined products at different temperatures for 2 h (**b**)

the product is observed. This indicates that the product is crystalline with a higher crystallinity. All the diffraction peaks in the pattern are in agreement with that of monoclinic $MnV_2O_6{\cdot}4H_2O$, with space group C2/c(15) and cell parameters: $a = 13.166$ nm, $b = 10.110$ nm, $c = 6.982$ nm, and density $= 2.496$ g cm^{-3}, from PDF card 86-0720. No diffraction peaks of other crystal phase, such as $MnV_2O_6{\cdot}2H_2O$, $MnV_2O_6{\cdot}H_2O$ and MnV_2O_6, are observed, which indicates that the solid⇄ solution equilibrium from the solid-state reaction conditions at low heat favors the evolution of three species to form the $MnV_2O_6{\cdot}4H_2O$ compound which is thermodynamically more stable at room temperature. The strong diffraction peak at about 11.4° for 2θ is attributed to the layered structure of $MnV_2O_6{\cdot}4H_2O$ with interlayer distance of 0.7769 nm.

From Fig. 1b, it can be found that XRD pattern of the calcined product at 418 K has a great difference in comparison with that of $MnV_2O_6{\cdot}4H_2O$, Such as, the diffraction peak at about 11.4° for 2θ disappeared when it was calcined at 418 K for 2 h, suggesting that the calcined product at 418 K is a non-layered structure compound. All the diffraction peaks in the pattern are in agreement with that of orthorhombic $MnV_2O_6{\cdot}2H_2O$, space group Pnma (62), cell parameters: $a = 5.609$ nm, $b = 10.917$ nm, $c = 12.042$ nm, density $= 2.747$ g cm^{-3}, from PDF card 70-3124.

When $MnV_2O_6{\cdot}4H_2O$ was heated over 673 K for 2 h, it can be found that two XRD patterns at 673 and 1123 K are similar except intensity of diffraction peaks, such as the calcined sample at 1123 K has more intensity diffraction peak at about 29.4° for 2θ than that of the calcined sample at 673 K, and all diffraction peaks in the two XRD patterns are found to be in agreement with that of monoclinic MnV_2O_6, space group C2/m (12), from PDF card 35-0139.

TG/DSC analysis of the synthetic product

Figure 2 shows the TG curve of the synthetic product at heating rate of 10 K min^{-1} from ambient temperature to 700 K. The TG curve shows that thermal decomposition of the $MnV_2O_6{\cdot}4H_2O$ below 700 K occurs in two well-defined steps. The first step starts at about 300 K, ends at about 390 K, which is attributed to the two water molecules eliminated from $MnV_2O_6{\cdot}4H_2O$ and the formation of $MnV_2O_6{\cdot}2H_2O$. The observed mass loss in the TG curve is 9.69%, which is in good agreement with 11.08% theoretic mass loss of two water molecules eliminated from $MnV_2O_6{\cdot}4H_2O$. The second decomposition step begins at about 390 K, and ends at 550 K, attributed to the decomposition of $MnV_2O_6{\cdot}2H_2O$ and the formation of MnV_2O_6. The corresponding observed mass loss in the TG curve is 9.54%, which closes to 11.08% theoretic mass loss of two water molecules eliminated from $MnV_2O_6{\cdot}2H_2O$.

Figure 3 shows the DSC curves of the synthetic product at four different heating rates from ambient temperature to 1140 K, respectively.

The DSC curve shows that the thermal process of the $MnV_2O_6{\cdot}4H_2O$ below 1140 K occurs in three obvious

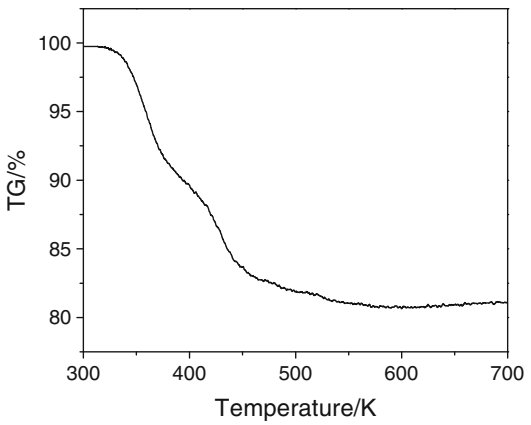

Fig. 2 TG curve of the $MnV_2O_6{\cdot}4H_2O$ at heating rate of 10 K min^{-1}

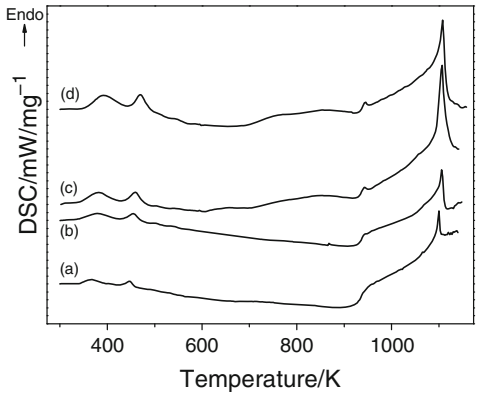

Fig. 3 DSC curves of the $MnV_2O_6{\cdot}4H_2O$ at heating rates of (*a*) 5 K min^{-1}, (*b*) 10 K min^{-1}, (*c*) 15 K min^{-1}, and (*d*) 20 K min^{-1}

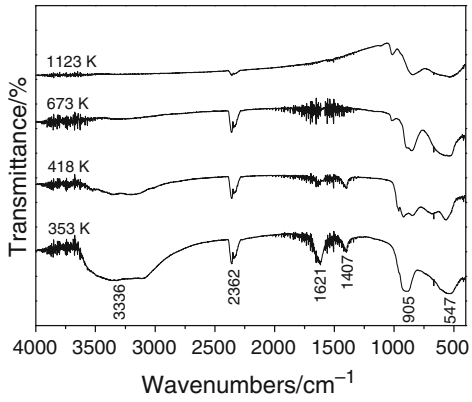

Fig. 4 IR spectra of $MnV_2O_6{\cdot}4H_2O$ at 353 K and its calcined samples at different temperatures

endothermic peaks. The weak endothermic DSC peak between 303 and 400 K is attributed to the dehydration of the two waters of crystallization from $MnV_2O_6{\cdot}4H_2O$ and the formation of $MnV_2O_6{\cdot}2H_2O$. The endothermic DSC peak between 400 and 500 K is assigned to the dehydration of the two waters of crystallization from $MnV_2O_6{\cdot}2H_2O$ and the formation of anhydrous MnV_2O_6, which are in agreement with that from the mass loss in the TG thermogram. The endothermic peak, which is located about 1105 K, is related to phase transition from solid phase MnV_2O_6 to liquid phase MnV_2O_6. Melting point of MnV_2O_6 is much lower than that of $MnNb_2O_6$ [25].

From Fig. 3, the peak temperature (T_P) is the temperature at which it attains its maximum, which is the endothermic peak temperature in the DSC curves. There is an upward shift in T_P of two step dehydration with increasing heating rate. However, T_P of phase transition from solid phase MnV_2O_6 to liquid phase MnV_2O_6 has few differences.

IR spectroscopic analysis of the product and its calcined samples

The FT-IR spectra of the product and its calcined samples are shown in Fig. 4. From Fig. 4, the strong and broad band at about 3336 cm^{-1} is assigned to the stretching OH vibration of the water molecule [20, 21], the weak band which appears at 1621 cm^{-1} in the spectrum of $MnV_2O_6{\cdot}4H_2O$ can be ascribed to the bending mode of the HOH [26–28]. The band at about 905 cm^{-1} is the vibrational mode of isolated V=O bonds in metavanadate group [29]. The band at 547 cm^{-1} can be attributed to ν(V–O–V) vibration of polymeric metavanadate [30, 31]. The bands at around 2362 and 1407 cm^{-1} should be assigned to the asymmetric and the symmetric stretching of CO_2(g), and the overlapping band at around 547 cm^{-1} is assigned to the bending mode of CO_2, which are attributed to the sample adsorbing CO_2 from air.

When $MnV_2O_6{\cdot}4H_2O$ is calcined at 418 K, the FT-IR spectra of the calcined sample $MnV_2O_6{\cdot}2H_2O$ have a little difference in comparison with that of $MnV_2O_6{\cdot}4H_2O$. Such as, the band at about 905 cm^{-1} of $MnV_2O_6{\cdot}4H_2O$ is split into three bands at 968, 924, and 842 cm^{-1} respectively, which is attributed that $MnV_2O_6{\cdot}4H_2O$ has monoclinic structure, however, the dihydrated compound is transformed into orthorhombic structure.

The FT-IR spectra of two calcined samples at 673 K and 1123 K are similar. However, two spectra have a great difference in comparison with that of $MnV_2O_6{\cdot}4H_2O$ or $MnV_2O_6{\cdot}2H_2O$. Such as, the band of MnV_2O_6 at about 3336 cm^{-1} disappears, and a new band at about 1020 cm^{-1} appears. It is explained by the fact that $MnV_2O_6{\cdot}4H_2O$ finishes elimination of its four waters of crystallization at 673 K. However, the cause that a new band of calcined sample above 673 K appears at about 1020 cm^{-1} is not clear.

SEM analysis of the synthetic product and its calcined samples

SEM micrographs of the synthesized $MnV_2O_6{\cdot}4H_2O$ and its calcined samples are shown in Fig. 5. A rod-like $MnV_2O_6{\cdot}4H_2O$ is shown in Fig. 5a, with diameter of about 250 nm, thickness of about 100 nm, and lengths up to 6 μm. After the calcined temperature is increased to 418 K, $MnV_2O_6{\cdot}2H_2O$ sample (Fig. 5b) can still keep rod-like morphology of $MnV_2O_6{\cdot}4H_2O$. However, diameter, thickness, and lengths of $MnV_2O_6{\cdot}2H_2O$ samples become smaller than that of $MnV_2O_6{\cdot}4H_2O$ samples. The calcined temperature is increased to 673 K further, the calcined sample MnV_2O_6 (Fig. 5c) is split into smaller rod-like particles. When $MnV_2O_6{\cdot}4H_2O$ is calcined at 1123 K for

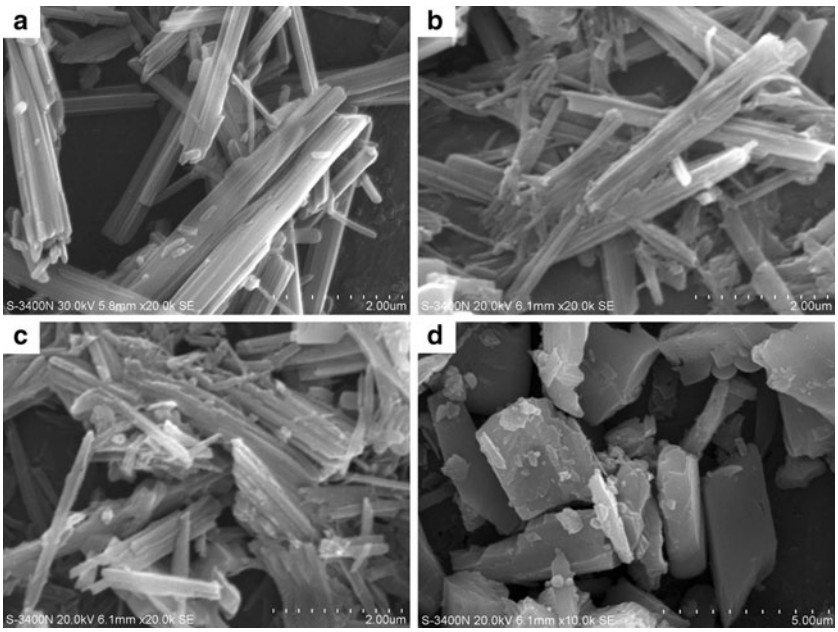

Fig. 5 SEM micrographs of $MnV_2O_6{\cdot}4H_2O$ at 353 K (**a**) and its calcined samples at 418 K (**b**), 673 K (**c**), and 1123 K (**d**)

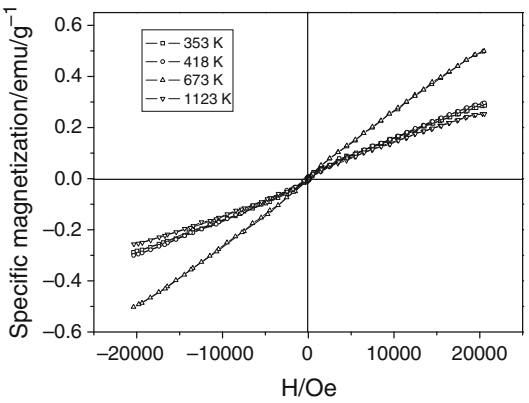

Fig. 6 The specific magnetization (M) as a function of field (H) of $MnV_2O_6{\cdot}4H_2O$ and its calcined samples at different temperatures for 2 h

2 h, morphology of the calcined sample, which has been ground, become block shapes (Fig. 5d).

Magnetic properties of the synthetic product and its calcined samples

The magnetic properties of $MnV_2O_6{\cdot}4H_2O$ and its calcined samples at different temperatures are shown in Fig. 6. It can be observed that the specific magnetization of all powders increases with the increase of applied field. The magnetic property of the sample obtained at 353 K is almost similar to that of the samples calcined at 418 and 1123 K, and the sample obtained at 673 K has larger specific magnetization than that of other samples under the same applied field. These samples show weak ferro- or ferrimagnetic behavior at room temperature.

Activation energy of thermal decomposition of $MnV_2O_6{\cdot}4H_2O$

In accordance with TG/DSC and XRD analysis of $MnV_2O_6{\cdot}4H_2O$ and its calcined products mentioned above, thermal process of $MnV_2O_6{\cdot}4H_2O$ below 1140 K consist of three steps, which can be expressed as follows:

$$MnV_2O_6 \cdot 4H_2O\ (cr) \rightarrow MnV_2O_6 \cdot 2H_2O\ (cr) + 2H_2O(g) \quad (6)$$

$$MnV_2O_6 \cdot 2H_2O\ (cr) \rightarrow MnV_2O_6(cr) + 2H_2O(g) \quad (7)$$

$$MnV_2O_6(cr) \rightarrow MnV_2O_6(l) \quad (8)$$

These thermal processes generate gaseous water or transformation of MnV_2O_6 from solid phase to liquid phase, so the change of the entropy of thermal processes will be positive. Therefore, as long as the temperature is high enough, the thermal processes mentioned above can occur spontaneously. Figure 7 shows Kissinger plots of the thermal decomposition of $MnV_2O_6{\cdot}4H_2O$. From the slopes of the straight lines, the activation energy values of two thermal decomposition steps of $MnV_2O_6{\cdot}4H_2O$ were determined to be 55.27 and 98.30 kJ mol^{-1}, respectively (Table 1). The step 2 exhibits higher activation energy value in comparison with steps 1, which suggests that dehydration of two waters of crystallization from $MnV_2O_6{\cdot}2H_2O$ is the rate-limiting step of the thermal decomposition of $MnV_2O_6{\cdot}4H_2O$.

Thermodynamics of thermal decomposition of $MnV_2O_6{\cdot}4H_2O$

Thermodynamic functions ($\Delta S^{\neq}$, $\Delta H^{\neq}$, and $\Delta G^{\neq}$) can be calculated from Eqs. 2–4, and the results are shown in

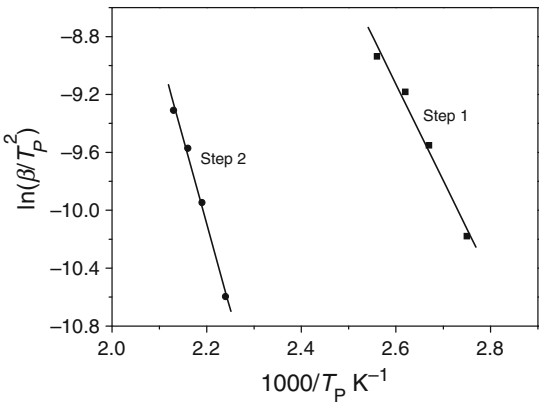

Fig. 7 Kissinger plots of the first and second dehydration steps of $MnV_2O_6{\cdot}4H_2O$

Table 1 Peak temperature (T_P) and kinetic parameters of thermal decomposition of $MnV_2O_6{\cdot}4H_2O$ obtained from Kissinger method

	Step 1	Step 2
T_p (K) in four heating rates/K min^{-1}		
5	363	447
10	375	457
15	382	464
20	390	470
E_a/kJ mol^{-1}	55.27	98.30
ln A	16.96	25.26
r^2	0.9919	0.9951

Table 2 Thermodynamic functions of the decomposition reaction of $MnV_2O_6{\cdot}4H_2O$

Parameters	Step 1	Step 2
$\Delta S^{\neq}$/J mol^{-1} K^{-1}	−114.45	−47.00
$\Delta H^{\neq}$/kJ mol^{-1}	52.03	94.39
$\Delta G^{\neq}$/kJ mol^{-1}	96.67	116.48

Table 2. It can be seen that the values of $\Delta S^{\neq}$ for step 1 and step 2 are negative. It shows that the corresponding activated complexes of two thermal decomposition processes have lower disorderness than the initial state. However, the entropy change of the second activated complex was higher than that of the preceding one. In terms of the theory of activated complex (transition theory), the step 1 of the thermal decomposition of $MnV_2O_6{\cdot}4H_2O$ may be interpreted as a ''slow'' stage, while the step 2 as a ''fast'' stage [24, 32, 33]. The positive values of $\Delta G^{\neq}$ for two steps of thermal decomposition are due to the fact that dehydration of the water of crystallization from $MnV_2O_6{\cdot}4H_2O$ can not occur spontaneously at room temperature. The larger $\Delta G^{\neq}$, the harder is decomposition process. So, the second decomposition process (step 2) occur harder than the first decomposition process (step 1), which is in agreement with experimental results. The endothermic peaks in DSC curve agree well with the positive sign of the activation enthalpy ($\Delta H^{\neq}$). The value of $\Delta H^{\neq}$ of the first decomposition process was smaller than that of the second decomposition process, which means that the first decomposition process needs less energy than the second decomposition process. In other words, $MnV_2O_6{\cdot}2H_2O$ is thermodynamically more stable than $MnV_2O_6{\cdot}4H_2O$ at elevated temperature.

Conclusions

This research has successfully achieved a selective self-assembly synthesis of $MnV_2O_6{\cdot}4H_2O$ with rod-like morphologies. XRD analysis suggests that $MnV_2O_6{\cdot}4H_2O$ is a compound with layered structure, and its calcined products $MnV_2O_6{\cdot}2H_2O$ and MnV_2O_6 are non-layered compounds. Magnetic characterization indicates that $MnV_2O_6{\cdot}4H_2O$ and its calcined products behave weak ferro- or ferrimagnetic behavior at room temperature. The thermal process of $MnV_2O_6{\cdot}4H_2O$ in the range of ambient temperature to 1140 K is a complex process, which involve the dehydration of the two waters of crystallization at first, and then dehydration of other two waters of crystallization, and at last melting of MnV_2O_6. The kinetics of the thermal decomposition of $MnV_2O_6{\cdot}4H_2O$ is studied using non-isothermal DSC technique. The average values of the activation energies associated with the $MnV_2O_6{\cdot}4H_2O$ thermal decomposition are 55.27 and 98.30 kJ mol^{-1} for the first and second steps, respectively. The thermodynamic functions ($\Delta S^{\neq}$, $\Delta H^{\neq}$, and $\Delta G^{\neq}$) of the decomposition reaction of $MnV_2O_6{\cdot}4H_2O$ are obtained. These data will be useful for further studies of the studied compound.

Acknowledgements This study was financially supported by the Guangxi Natural Scientific Foundation of China (Grant No. 2011GXNSFA018036), and the Guangxi Science and Technology Agency Research Item of China (Grant No. 0992001-5).

References

1. Valanarasu S, Chandramohan R. Effect of Pb doping on structural and electrochemical properties of combustion synthesised $LiCoO_2$ powder. J Mater Sci. 2010;45:2317–23.
2. Arai H, Tsuda M, Saito K, Hayashi M, Sakurai Y. Thermal reactions between delithiated lithium nickelate and electrolyte solutions. J Electrochem Soc. 2002;149:401–6.
3. Park BG, Kim S, Kim ID, Park YJ. Structural and electrochemical performance of three-dimensional $LiMn_2O_4$ thin film. J Mater Sci. 2010;45:3947–53.

4. Xiang HF, Wang H, Chen CH, Ge XW, Guo S, Sun JH, Hu WQ. Thermal stability of $LiPF_6$-based electrolyte and effect of contact with various delithiated cathodes of Li-ion batteries. J Power Sources. 2009;191:575–81.
5. Wang YD, Jiang JW, Dahn JR. The reactivity of delithiated $Li(Ni_{1/3}Co_{1/3}Mn_{1/3})O_2$, $Li(Ni_{0.8}Co_{0.15}Al_{0.05})O_2$ or $LiCoO_2$ with non-aqueous electrolyte. Electrochem Commun. 2007;9:2534–40.
6. Kim SS, Ikuta H, Wakihara M. Synthesis and characterization of MnV_2O_6 as a high capacity anode material for a lithium secondary battery. Solid State Ion. 2001;139:57–65.
7. Liu HW, Tang DG. Synthesis of ZnV_2O_6 powder and its cathodic performance for lithium secondary battery. Mater Chem Phys. 2009;114:656–9.
8. Andrukaitis E, Cooper JP, Smit JH. Lithium intercalation in divalent metal vanadates MeV_2O_6 (Me = Cu, Co, Ni, Mn or Zn). J Power Sources. 1995;54:465–9.
9. Cao XY, Xie JG, Zhan H, Zhou YH. Synthesis of CuV_2O_6 as a cathode material for rechargeable lithium batteries from V_2O_5 gel. Mater Chem Phys. 2006;98:71–5.
10. Ni SB, Zhou G, Wang XH, Sun XL, Yang F, Liu YQ, He DY. Synthesis of $Zn_3(OH)_2V_2O_7{\cdot}nH_2O$ hierarchical nanostructures and their photoluminescence properties. Mater Chem Phys. 2010;120:426–30.
11. Hara D, Shirakawa J, Ikuta H, Uchimoto Y, Wakihara M, Miyanaga T, Watanabe I. Charge–discharge reaction mechanism of manganese vanadium oxide as a high capacity anode material for lithium secondary battery. J Mater Chem. 2002;12:3717–22.
12. Manivannan V, Parhi P, Howard J. Mechanochemical metathesis synthesis and characterization of nano-structured $MnV_2O_6{\cdot}xH_2O$ ($x = 2, 4$). J Cryst Growth. 2008;310:2793–9.
13. Leroux F, Piffard Y, Ouvrard G, Mansot JL, Guyomard D. New amorphous mixed transition metal oxides and their Li derivatives: synthesis, characterization, and electrochemical behavior. Chem Mater. 1999;11:2948–59.
14. Liao JH, Leroux F, Drezen T, Guyomard D, Piffard Y. Synthesis, structures and thermal analysis of $MnV_2O_6{\cdot}nH_2O$ ($n = 1, 2$ and 4). Eur J Solid State Inorg Chem. 1996;33:411–27.
15. Morishita T, Nomura K, Inamasu T, Inagaki M. Synthesis of anhydrous manganese vanadate powder by coprecipitation and its anodic performance for lithium secondary battery. Solid State Ion. 2005;176:2235–41.
16. Takahiro Morishita T, Konno H, Izumi Y, Inagaki M. Oxidation state of vanadium in amorphous MnV_2O_6 formed during discharge–charge cycle and the improvement of its synthesis condition. Solid State Ion. 2006;177:1347–53.
17. Liu Y, Zhang YG, Du J, Yu WC, Qian YT. Synthesis and characterization of single-crystal MnV_2O_6 nanobelts. J Cryst Growth. 2006;291:320–4.
18. Parhi P, Manivannan V. Novel solution phase metathetic pathway for the synthesis of $MnV_2O_6{\cdot}H_2O$. Mater Res Bull. 2008;43:2966–73.
19. Huang WD, Gao SK, Ding XK, Jiang LL, Wei MD. Crystalline MnV_2O_6 nanobelts: synthesis and electrochemical properties. J Alloys Compd. 2010;495:185–8.
20. Wu WW, Wu XH, Lai SB, Liao S. Non-isothermal kinetics of thermal decomposition of $NH_4ZrH(PO_4)_2{\cdot}H_2O$. J Therm Anal Calorim. 2010. doi:10.1007/s10973-010-0986-3.
21. Wu XH, Wu WW, Li SS, Cui XM, Liao S. Kinetics and thermodynamics of thermal decomposition of $NH_4NiPO_4{\cdot}6H_2O$. J Therm Anal Calorim. 2011;103:805–12.
22. Kissinger HE. Reaction kinetics in differential thermal analysis. Anal Chem. 1957;29:1702–6.
23. Boonchom B, Puttawong S. Thermodynamics and kinetics of the dehydration reaction of $FePO_4{\cdot}2H_2O$. Phys B. 2010;405:2350–5.
24. Vlaev L, Nedelchev N, Gyurova K, Zagorcheva M. A comparative study of non-isothermal kinetics of decomposition of calcium oxalate monohydrate. J Anal Appl Pyrolysis. 2008;81:253–62.
25. Mansurova AN, Gulyaeva RI, Chumarev VM, Mar'evich VP. Thermochemical properties of $MnNb_2O_6$. J Therm Anal Calorim. 2010;101:45–7.
26. Wu XH, Wu WW, Liu C, Li SS, Liao S, Cai JC. Synthesis of layered sodium manganese phosphate via low-heating solid-state reaction and its properties. Chin J Chem. 2010;28:2394–8.
27. Boonchom B, Danvirutai C, Maensiri S. Soft solution synthesis, non-isothermal decomposition kinetics and characterization of manganese dihydrogen phosphate dihydrate $Mn(H_2PO_4)_2{\cdot}2H_2O$ and its thermal transformation products. Mater Chem Phys. 2008;109:404–10.
28. Liu C, Wu XH, Wu WW, Cai JC, Liao S. Preparation of nanocrystalline $LiMnPO_4$ via a simple and novel method and its isothermal kinetics of crystallization. J Mater Sci. 2011;46:2474–8.
29. Ceccato R, Carturan G, Decker F, Artuso F. Sol-gel synthesis of vanadate-based thin films as counter electrodes in electrochromic devices. J Sol-Gel Sci Technol. 2003;26:1071–4.
30. Rodella CB, Franco RWA, Magon CJ, Donoso JP, Nunes LAO, Saeki MJ, Aegerter MA, Sargentelli V, Florentino AO. V_2O_5/TiO_2 catalytic xerogels Raman and EPR studies. J Sol-Gel Sci Technol. 2002;25:83–8.
31. Beg S, Al-Alas A, Al-Areqi NAS. Study on structural and electrical properties of layered perovskite-type oxide-ion conductor. Mater Chem Phys. 2010;124:305–11.
32. Boonchom B. Kinetics and thermodynamic properties of the thermal decomposition of manganese dihydrogenphosphate dihydrate. J Chem Eng Data. 2008;53:1533–8.
33. Danvirutai C, Noisong P, Youngme S. Some thermodynamic functions and kinetics of thermal decomposition of $NH_4MnPO_4{\cdot}H_2O$ in nitrogen atmosphere. J Therm Anal Calorim. 2010;100:117–24.